ChemPhotoChem

Chemistry Europe
European Chemical Societies Publishing

RESEARCH ARTICLE

A Complementary Theoretical Study on 6-Nitro BIPS Spiropyran Photoswitching Mechanism

Zsuzsánna Bálint[1] | Attila Bende[2]

[1]Faculty of Physics, Babeş-Bolyai University, Cluj, Romania | [2]Isotopic and Molecular Technologies Department, National Institute of R&D of Isotopic and Molecular Technology, Cluj-Napoca, Romania

Correspondence: Attila Bende (attila.bende@itim-cj.ro)

Received: 29 July 2025 | **Revised:** 11 November 2025 | **Accepted:** 19 November 2025

Keywords: conical intersection | excited-state relaxation | merocyanine | spin-flipped time-dependent density functional theory | spiropyran

ABSTRACT

The photochromic interconversion between spiropyran (SP) and merocyanine (MC) was investigated using density functional theory (DFT) and its linear-response time-dependent extension. Equilibrium and transition-state geometries in both the ground and electronically excited states were optimized using the ωB97X-D3BJ exchange-correlation functional, combined with empirical dispersion corrections, the conductor-like polarizable continuum model for solvation, and the def2-TZVPP triple-ζ basis set. Conical intersection geometries were located using the spin-flip TDDFT approach. Key molecular configurations, including equilibrium, transition-state, and conical intersection geometries, were mapped along the SP–MC interconversion, and the energetically most favorable relaxation pathways were determined. The results also demonstrate that the relaxation pathway through the triplet manifold could be a possible alternative. The influence of the solvent environment on UV–vis absorption, excited-state relaxation, and SP–MC interconversion was emphasized. Finally, the efficiency of the full back-and-forth SP–MC transformation, induced by either light or thermal effects, was characterized in both vacuum and polar environments.

1 | Introduction

Photoswitches are molecular systems that can reversibly change theirstructure in response to external stimuli, particularly when irradiated with light of a specific wavelength [1]. Such systems enable the development of novel materials whose physical or chemical properties can be tuned through controlled geometrical configurations [2–10].

A representative example of this class is the photochromic interconversion between spiropyran (SP) and merocyanine (MC) [11] (see Scheme 1), which exhibits a characteristic photoswitching behavior. The SP–MC system has been widely employed in developing technological applications, including optical data storage [12], optical switches [13, 14], nanoparticles [15], photonic crystals [16], light-driven smart materials [17–19], information encryption [20, 21], and various biological systems [22, 23].

Experimentally, the reversible photochemical process between SP and MC has been shown to occur through a sequence of distinct steps. Upon light absorption and subsequent excitation of SP, the C—O bond is broken along the excited-state relaxation pathway, resulting in the opening of the 2*H*-benzopyran ring. Next, a rotation around one of the C—C bonds leads to the formation of the MC conformation. The reverse transformation, which does not necessarily require photoexcitation but can proceed thermally, begins with a similar rotation about the C—C bond, reconstructing the ring structure and regenerating the SP form.

During this SP $\rightleftharpoons$ MC interconversion, several photochemical characteristics have been experimentally identified. For instance, the reaction rate and yield depend on the solvent, both for the MC → SP back transformation [24] and the SP → MC ring-opening photoreaction [25]. Moreover, a faster MC → SP conversion is observed under light irradiation than under purely thermal conditions [26]. Finally, substituents attached to the nitrogen sites of the indoline ring can significantly alter the photochemical response of SP [21, 27–30].

A precise theoretical description of the photochromic ring-opening process has long been the subject of active debate.

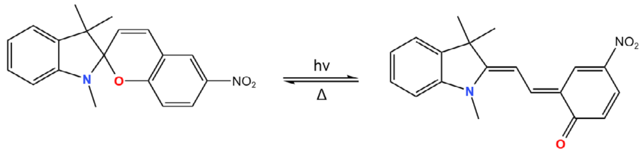

SCHEME 1 | The interconversion between SP and MC mediated by UV-light and thermal effects.

Earlier studies, employing either simplified benzopyran model systems [31, 32] or the full SP molecular structure [33–36], have proposed several possible relaxation mechanisms. However, no comprehensive theoretical studies have yet been published that also take radiationless relaxations into account in the interconversion mechanism between SP and MC. In these studies, the NO_2 substituent on the benzopyran ring was often omitted, or lower-level theoretical methods were applied [37], while some focused primarily on comparing the performance of different exchange-correlation functionals [38, 39].

The aim of this work is to provide a detailed ab initio theoretical description of the complete SP ⇌ MC interconversion and to elucidate the photochemical behavior of each stage, including UV absorption, radiative and nonradiative relaxation of excited states, and structural relaxation processes.

2 | Results and Discussion

2.1 | SP to MC Conversion

2.1.1 | Absorption

The equilibrium geometries of the ground state and the corresponding vibrational normal modes of the SP and MC conformations were optimized in both vacuum and polar environments at the *ω*B97X-D3BJ/def2-TZVPP/conductor-like polarizable continuum model (CPCM) level of theory, without imposing any geometry constraints. The optimized ground-state geometry of SP is shown in Figure 1, and the atomic coordinates are provided in the Supporting Information, (Figure S1, Supporting Information). As illustrated in Figure 1, the spatial structure of SP consists of two planar fragments – 6-nitro-2H-benzopyran (BP) and 2,3-dihydro-1,3,3-trimethylindole (DHTI) – tetrahedrally linked through the common carbon atom C_1.

Vertical excitation energies and oscillator strengths were calculated using the *ω*B97X-D3BJ/def2-TZVPP method in both vacuum and polar environments. For comparison, additional calculations were carried out with the SOS-PBE-QIDH double-hybrid exchange-correlation (XC) functional, which incorporates a spin-opposite scaled second-order perturbative correction to enhance the description of electron correlation. Accordingly, four computational setups were defined: M1, *ω*B97X-D3BJ/def2-TZVPP/(vacuum); M2, *ω*B97X-D3BJ/def2-TZVPP/CPCM (water); M3, SOS-PBE-QIDH/def2-TZVPP/(vacuum); and M4, SOS-PBE-QIDH/def2-TZVPP/CPCM(water). The first five excitation wavelengths of SP, together with their oscillator strengths, are summarized in Table 1, whereas selected geometric parameters (particularly the equilibrium bond lengths $R_e(S_0)^{SP}$) of the photochemically active 2*H*-pyran fragment are listed in Table 2. The oscillator strengths obtained using the M1 method (*ω*B97X-D3BJ/def2-TZVPP in vacuum) indicate that the S_1 and S_2 transitions are either dark or only weakly allowed, whereas strong absorption occurs for the $S_0 \rightarrow S_3$ transition and higher. In a polar environment (M2 method), however, the intensity of the $S_0 \rightarrow S_2$ transition increases significantly, revealing a clear solvent effect.

The more advanced SOS-PBE-QIDH XC functional further modifies the spectral pattern, producing both wavelength shifts and changes in the absorption intensity. The origin of these changes can be elucidated by analyzing the natural difference orbital (NDO) profiles associated with each excitation [40, 41].

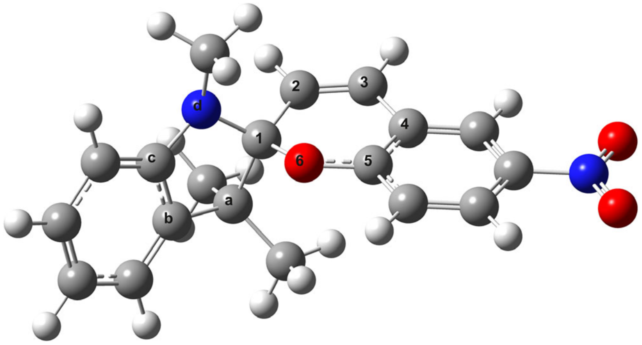

FIGURE 1 | The ground state equilibrium geometry of SP obtained at the *ω*B97X-D3BJ/def2-TZVPP level of theory.

TABLE 1 | The first five electronic excited-state wavelengths (in nm) of SP, with oscillator strengths given in parentheses, the corresponding fragment localizations and the electronic transition character computed at four levels of theory: **M1** - *ω*B97X-D3BJ/def2-TZVPP/(vacuum), **M2** - *ω*B97X-D3BJ/def2-TZVPP/CPCM(water), **M3** - SOS-PBE-QIDH/def2-TZVPP/(vacuum) and **M4** - SOS-PBE-QIDH/def2-TZVPP/CPCM(water).

State	M1	M2	M3	M4
$\lambda(S_1)$	293	292	304	307
	(0.0000)	(0.0008)	(0.0000)	(0.2139)
	NO_2	NO_2	NO_2	BP
	$n \rightarrow \pi^*$	$n \rightarrow \pi^*$	$n \rightarrow \pi^*$	$\pi \rightarrow \pi^*$
$\lambda(S_2)$	261	275	285	304
	(0.0005)	(0.3147)	(0.0904)	(0.0003)
	NO_2	BP	BP	NO_2
	$n \rightarrow \pi^*$	$\pi \rightarrow \pi^*$	$\pi \rightarrow \pi^*$	$n \rightarrow \pi^*$
$\lambda(S_3)$	261	263	278	285
	(0.0345)	(0.0169)	(0.0925)	(0.2068)
	BP	BP	BP	BP
	$\pi \rightarrow \pi^*$	$\pi \rightarrow \pi^*$	$\pi \rightarrow \pi^*$	$\pi \rightarrow \pi^*$
$\lambda(S_4)$	257	256	274	284
	(0.1464)	(0.0003)	(0.0497)	(0.0181)
	BP	NO_2	NO_2	NO_2
	$\pi \rightarrow \pi^*$	$n \rightarrow \pi^*$	$n \rightarrow \pi^*$	$n \rightarrow \pi^*$
$\lambda(S_5)$	242	245	271	274
	(0.0966)	(0.06292)	(0.0150)	(0.0431)
	DHTI	DHTI	DHTI	DHTI → BP
	$\pi \rightarrow \pi^*$	$\pi \rightarrow \pi^*$	$\pi \rightarrow \pi^*$	$\pi \rightarrow \pi^*$

TABLE 2 | The bond lengths (in Å) of the 2*H*-pyran six-membered ring fragment for different equilibrium (R_e), conical intersection (*ci*) and transition-state (TS) geometries along with their relative energies (in eV) computed at the ωB97X-D3BJ/def2-TZVPP level of theory in both vacuum and polar environments.

Nr.	Geom.	C_1-C_2	C_2-C_3	C_3-C_4	C_4-C_5	C_5-O_6	C_1-O_6	C_2-O_6	En.
2*H*-pyran fragment in SP and MC in vacuum									
1	$R_e(S_0)^{SPa}$	1.496	1.325	1.455	1.397	1.340	1.455	—	0.00
2	$R_e(S_0)^{MC}$	1.375	1.395	1.384	1.474	1.230	—	2.837	0.77
3	$R_e(S_1)^a$	1.496	1.325	1.455	1.396	1.345	1.450	—	3.39
4	$R_e(S_1)^b$	1.415	1.372	1.427	1.452	1.260	2.469	2.686	3.38
5	$R_e(S_1)^c$	1.388	1.443	1.398	1.443	1.270	2.706	2.255	3.20
6	$R_e(S_1)^d$	1.387	1.382	1.432	1.474	1.250	—	2.672	3.69
7	$ci(S_3 \times S_2)$	1.483	1.344	1.428	1.434	1.355	1.456	—	4.57
8	$ci(S_2 \times S_1)$	1.448	1.362	1.419	1.445	1.297	1.749	2.534	4.44
9	$ci(S_1 \times S_0)^a$	1.501	1.473	1.395	1.413	1.365	2.323	1.456	3.72
10	$ci(S_1 \times S_0)^b$	1.396	1.353	1.490	1.485	1.226	—	—	3.51
11	TS^1	1.382	1.427	1.392	1.457	1.261	2.490	2.472	3.64
12	TS^2	1.378	1.406	1.413	1.468	1.258	3.368	2.511	3.75
13	TS^3	1.334	1.463	1.347	1.497	1.214	3.275	2.840	1.53
2*H*-pyran fragment in Benzopyran in vacuum									
14	$ci(S_1 \times S_0)^i$	1.413	1.472	1.361	1.435	1.283	2.589	1.709	—
15	$ci(S_1 \times S_0)^{ii}$	1.352	1.404	1.464	1.412	1.272	—	—	—
2*H*-pyran fragment in 6-Nitro-Benzopyran in vacuum									
16	$ci(S_1 \times S_0)^i$	1.409	1.471	1.363	1.441	1.277	2.614	1.754	—
17	$ci(S_1 \times S_0)^{ii}$	1.350	1.403	1.453	1.437	1.248	—	—	—
2*H*-pyran fragment in SP and MC in water									
18	$R_e(S_0)^{SP}$	1.495	1.325	1.456	1.398	1.338	1.460	—	0.00
19	$R_e(S_0)^{MC}$	1.410	1.363	1.423	1.457	1.247	—	2.868	0.35
20	$R_e(S_1)^a$	1.495	1.325	1.456	1.397	1.345	1.455	—	3.46
21	$R_e(S_1)^b$	1.460	1.330	1.462	1.468	1.234	2.588	2.973	3.74
22	$R_e(S_1)^c$	1.394	1.406	1.398	1.474	1.245	2.746	2.730	3.26
23	$R_e(S_1)^d$	1.386	1.400	1.407	1.485	1.238	—	2.815	3.08
24	$ci(S_2 \times S_1)$	1.485	1.334	1.436	1.435	1.311	1.474	2.446	4.02
25	$ci(S_1 \times S_0)^a$	1.496	1.471	1.390	1.420	1.354	2.334	1.471	3.73
26	$ci(S_1 \times S_0)^b$	1.381	1.382	1.492	1.496	1.211	—	—	3.54
27	TS^1	1.391	1.421	1.395	1.470	1.249	2.685	2.594	3.75
28	TS^2	1.385	1.431	1.400	1.463	1.254	—	2.483	3.38
29	TS^3	1.335	1.464	1.350	1.490	1.221	3.387	2.886	1.39

[a] $\mathbf{TS^1}$: $R_e(S_1)^b \wedge R_e(S_1)^c$; $\mathbf{TS^2}$: $R_e(S_1)^c \wedge R_e(S_1)^d$; $\mathbf{TS^3}$: $R_e(S_0)^{SP} \wedge R_e(S_0)^{MC}$.

Accordingly, the NDO profiles were calculated for the first five excited states, using all four computational setups (M1-M4), and the corresponding profiles are reported in the Supporting Information (Tables S1-S4). Notably, when the ωB97X-D3BJ functional is employed, the order of the S_2 and S_4 states is reversed in a polar environment (see the second and third columns in Table 1). Furthermore, within the SOS-PBE-QIDH framework, which includes a perturbative correlation component, substantial oscillator strength is already observed for S_1 transition in water (see fifth column in Table 1). These observations indicate that the solvent environment can significantly alter both the position and intensity of absorption peaks in the UV spectrum, in agreement with experimental findings [24]. Furthermore, it is important to note that the position of absorption peaks depends strongly on solvent polarity

[42]. This means more than just a shift in the spectrum; as can be seen in Table 1, it also involves a reversal of the order of the excited states. More precisely, if one analyzes the nature of the excitations, the first two states obtained in a vacuum environment, when considering the ωB97X-D3BJ functional, are localized on the NO_2 fragment and are of $n \rightarrow \pi^*$ character. The third and fourth states are largely localized to the NO_2 and benzopyran fragments and are $\pi \rightarrow \pi^*$ in character, while the fifth state is associated with the DHTI (or indoline) fragment and is also $\pi \rightarrow \pi^*$ in nature, showing both a local (indoline to indoline) and a delocalized (indoline to benzopyran) electron transition. It should also be noted that the chosen method can cause interesting changes in the order of the excited states. For instance, when comparing the results obtained using the M1 and M3 methods, one can see that the S_2 state, originally the second excited state, appears as S_4 in the spectrum, considering the M3 method.

2.1.2 | Excited-State Relaxation: Benzopyran Channel

In vacuum. As shown in the subsection absorption, for the M1 computational setup, the S_1 and S_2 electronic states are difficult to access due to their negligible or very weak oscillator strengths. However, in general, an important step in the excited-state relaxation from higher states is the relaxation to S_1, which is typically fast from a photochemical perspective. Following a less probable $S_0 \rightarrow S_1$ vertical excitation, the system relaxes to an equilibrium geometry in which only the geometric parameters of the NO_2 fragment change, whereas no significant rearrangements occur in the photochemically active 2*H*-pyran or the DHTI fragments. The corresponding bond parameters are listed in Table 2 under the label $R_e(S_1)^a$, and the optimized molecular structure is shown in Figure S2 of the Supporting Information. In this configuration, the N—C bond connecting the NO_2 fragment to the pyran ring shortens from 1.463 Å (in the ground state) to 1.379 Å (in the excited state). Relaxation initiated after an $S_0 \rightarrow S_3$ vertical excitation follows a different pathway. The S_3 state descends on its potential energy surface until it reaches the $S_3 \times S_2$ conical intersection, denoted $ci(S_3 \times S_2)$. The primary geometrical change between the S_0 and $ci(S_3 \times S_2)$ structures occurs in the $C_4{-}C_5$ bond, which elongates from 1.397 to 1.434 Å whie other bonds in the 2*H*-pyran ring remain largely unchanged. From this intersection, the system proceeds downhill to $ci(S_2 \times S_1)$, and then to the equilibrium geometries $R_e(S_1)^b$ and $R_e(S_1)^c$. This relaxation channel (S_3–$ci(S_3 \times S_2)$–$ci(S_2 \times S_1)$–$R_e(S_1)^b$–$R_e(S_1)^c$) is energetically favorable, with successive decreases from 4.75 to 4.57 eV, 4.44 eV, 3.38 eV, and finally 3.20 eV. A small energy barrier (TS^1 with a height of 0.26 eV, 5.996 kcal/mol) is encountered during the $R_e(S_1)^b \rightarrow R_e(S_1)^c$ transition. Geometrically, this process involves shortening of the $C_1{-}C_2$, $C_4{-}C_5$ and $C5{-}O_6$ bonds, and elongation of the $C_2{-}C_3$ and $C_1{-}O_6$ bonds. In particular, the latter bond stretches from 1.749 to 2.706 Å, clearly indicating the opening of the six-membered 2*H*-pyran ring. The corresponding molecular structures of $ci(S_3 \times S_2)$, $ci(S_2 \times S_1)$, $R_e(S_1)^b$, $R_e(S_1)^c$, and TS^1 are presented in Figures S3–S7 of the Supporting Information. Finally, the system decays from $R_e(S_1)^c$ to the ground state through the critical crossing $ci(S_1 \times S_0)$, computed using the spin-flip TDDFT (SF-TDDFT) method. This is no longer a spontaneous transition but one that proceeds over the energy barrier (0.52 eV) defined by the critical point.

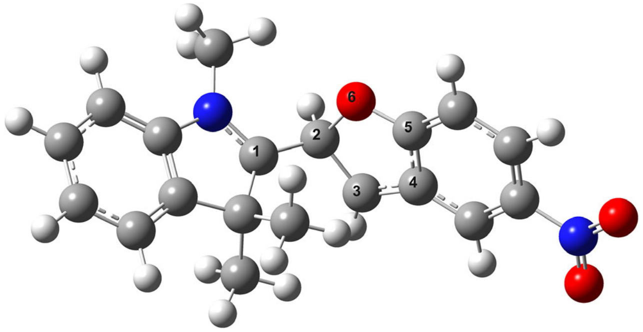

FIGURE 2 | The $ci(S_1 \times S_0)^a$ conical intersection geometry for SP obtained at the SF-TDDFT/ωB97X-D3BJ/def2-TZVPP level of theory.

The corresponding geometry, $ci(S_1 \times S_0)^a$, is shown in Figure 2 and in Figure S8 of the Supporting Information, and the associated bond parameters for the 2*H*-pyran fragment are listed in the ninth row of Table 2. As seen in Figure 2, the previously open six-membered ring collapses to a five-membered ring, forming a new $C_2{-}O_6$ bond of 1.456 Å. This *ci* geometry differs from that found for benzopyran [31, 32], where an open-ring configuration was reported for $ci(S_1 \times S_0)$. Because SF-TDDFT is not yet widely adopted for conical intersection optimization due to known theoretical limitations [43], a validation was performed by locating the $ci(S_1 \times S_0)$ crossing in benzopyran using SF-TDDFT and comparing it with NEVPT2 results. Consequently, the $S_1 \times S_0$ crossing geometry for benzopyran, obtained using the SF-TDDFT/ωB97X-D3BJ/def2-TZVPP method, exhibits a closed five-membered ring structure similar to that found for SP. The corresponding molecular structure is shown in Figure 3 (atomic coordinates given in Figure S9 of the Supporting Information), and the associated bond parameters are listed in Table 2 under the label $ci(S_1 \times S_0)^i$ (row 14).

Comparison of Figures 2 and 3, as well as the bonding parameters of the $ci(S_1 \times S_0)^a$ and $ci(S_1 \times S_0)^i$ geometries in Table 2 (rows 9 and 14), reveals very good agreement between the two structures. The only noticeable difference is in the $C_2{-}O_6$ bond length (1.456 Å vs. 1.709 Å), but the configuration of the five-membered ring remains unaffected. For the NEVPT2 calculation, a configuration with ten electrons in ten active orbitals was used, corresponding to one-electron excitation between five occupied and five virtual orbitals. Of the five occupied orbitals, three are pure π orbitals localized on the benzene ring, while the other two are a mixture of σ and π orbitals belonging to the five-membered ring. Three of the five virtual orbitals are also pure π^* antibonding

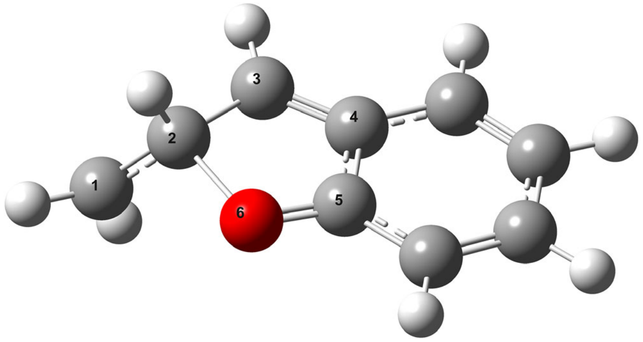

FIGURE 3 | The closed-form $ci(S_1 \times S_0)^i$ conical intersection geometry for benzopyran obtained at the SF-TDDFT/ωB97X-D3BJ/def2-TZVPP level of theory.

orbitals localized on the benzene ring, whereas the other two are a mixture of valence- and Rydberg-type orbitals that partly belong to the five-membered ring and are widely spread in the space around the ring. During excitation, the occupancy of the last two virtual orbitals was low; however, their presence helped stabilize the convergence of the CASSCF method. The multireference CASSCF results, without including electron correlation, yield an excitation energy of 0.662 eV (0.024 au) for the S_1 state, which decreases to 0.044 eV (0.0016 au) when electron correlation is included through the NEVPT2 method. This relatively low energy suggests that the *ci* geometry of benzopyran obtained with SF-TDDFT is realistic and supports the validity of the $ci(S_1 \times S_0)^a$ geometry obtained for SP. The *ci* geometry was recomputed for 6-nitro benzopyran using the SF-TDDFT method and then compared with the NEVPT2 results (Figure S10). For the SF-TDDFT, there were no significant differences in the bond lengths compared to the unsubstituted system, with the greatest change observed in the distance of C_2—O_6 (1.709 Å vs. 1.754 Å). For more details, see rows 14 and 16 in Table 2. In the CASSCF and NEVPT2 multi-reference single point calculations, the presence of the NO_2 fragment was accounted by including one additional occupied orbital in the active space, resulting in an (11*o*,12*e*) configuration. The S_1 - S_0 energy gap computed with the CASSCF method is 0.74 eV, while the NEVPT2 method yields a value of 0.008 eV. Once again, the latter value proves that results obtained with SF-TDDFT are highly reliable.

Following the relaxation path, a ground-state optimization was performed using the $ci(S_1 \times S_0)^a$ geometry as the starting structure. The optimization showed that the system returns to the closed, six-membered ring form, corresponding to the $R_e(S_0)^{SP}$ geometry.

If, however, the molecule continues to rotate from the $R_e(S_1)^c$ equilibrium geometry along the C_2–C_3 axis, it can easily access another conical intersection geometry, denoted $ci(S_1 \times S_0)^b$. The corresponding molecular structure is shown in Figure 4, while the associated bond parameters are listed in Table 2 (row 10) under the geometry label $ci(S_1 \times S_0)^b$, and the atomic coordinates are given in the Supporting Information (Figure S11). The transition from $R_e(S_1)^c$ to this *ci* geometry is energetically more favorable than in the previous case, as the barrier is 0.2 eV lower.

To validate this structure, benchmark calculations were also performed for the $ci(S_1 \times S_0)^b$ geometry using the benzopyran model system. The corresponding $S_1 \times S_0$ crossing geometry of benzopyran was computed using the SF-TDDFT/ωB97X-D3BJ/def2-TZVPP method, starting from the zig–zag configuration of the unsaturated carbon chain found within the $ci(S_1 \times S_0)^b$ geometry of SP. The resulting bond parameters for the benzopyran 2*H*-pyran fragment are reported in Table 2 (row 15) under the label $ci(S_1 \times S_0)^{ii}$, and the corresponding molecular structure is shown in Figure 5. The atomic coordinates are listed in Figure S12 of the Supporting Information. A comparison of Figures 4 and 5, shows that the overall shapes of the two *ci* geometries are very similar, with only small variations in bond distances (see rows 10 and 15 in Table 2). Subsequently, a single-point NEVPT2 calculation was carried out using the same active orbital configuration as in the previous case. The multireference CASSCF results without electron correlation yield an S_1 excitation energy of 0.608 eV (0.022 au), which decreases to 0.132 eV (0.0048 au) when electron correlation is included at the NEVPT2 level. As in the $ci(S_1 \times S_0)^i$ case, the presence of the 6-nitro group was taken into account when computing the *ci* geometry. Compared to the system without the 6-nitro substituent, slight changes were observed in the C_4—C_5 and C_5—C_6 bond lengths, but no structural rearrangements were found (See rows 15 and 17 in Table 2). In the CASSCF multi-reference calculations, an (11*o*,12*e*) active space was used, yielding an $S_0 \rightarrow S_1$ excitation energy of 0.74 eV. In comparison, the NEVPT2 method gave a value of 0.009 eV. Although the NEVPT2 result is close to the SF-TDDFT value, the S_1 excitation energy remains slightly larger, which prevents us from definitively confirming that the present *ci* geometry is valid according to both methods. Further calculations would be required to localize the true *ci* geometry using the NEVPT2 approach, but this is not feasible due to the lack of gradients. However, the close numerical agreement between the two approaches suggests that the SF-TDDFT *ci* geometry is a reliable approximation.

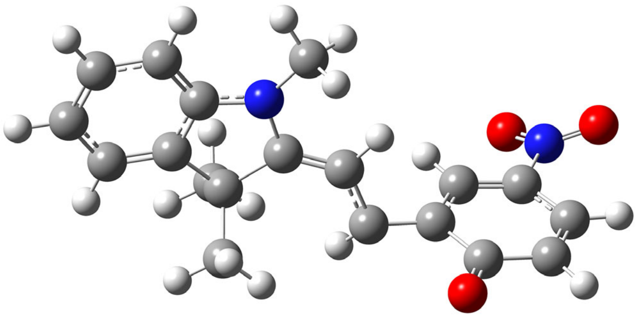

FIGURE 4 | The $ci(S_1 \times S_0)^b$ conical intersection geometry for SP obtained at the SF-TDDFT/ωB97X-D3BJ/def2-TZVPP level of theory.

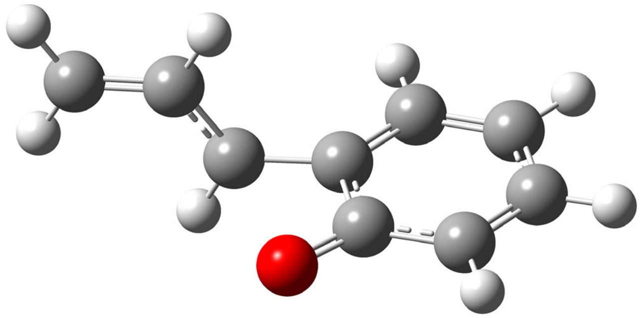

FIGURE 5 | The open-form $ci(S_1 \times S_0)^{ii}$ conical intersection geometry for benzopyran obtained at the SF-TDDFT/ωB97X-D3BJ/def2-TZVPP level of theory.

Continuing along the relaxation pathway, a ground-state optimization starting from $ci(S_1 \times S_0)^b$ leads to the $R_e(S_0)^{MC}$ geometry, demonstrating that the photoswitching proceeds through the conversion from the SP to the MC configuration. The MC conformation is shown in Figure S14 of the Supporting Information.

As for radiative relaxation, the fluorescence emission wavelengths calculated for the first excited-state equilibrium geometries are as follows: at the ωB97X-D3BJ/def2-TZVPP level of theory the predicted wavelengths are 512 nm for $R_e(S_1)^a$, 656 nm for $R_e(S_1)^b$, and 659 nm for $R_e(S_1)^c$. At the SOS-PBE-QIDH/def2-TZVPP level, the corresponding values are 575, 874, and 882 nm, respectively. The theoretical estimate of the fluorescence lifetime was possible only for $R_e(S_1)^a$, where the harmonic approximation remains valid in the framework of Fermi's Golden Rule. Accordingly, the calculated fluorescence lifetime along the $R_e(S_1)^a$ relaxation pathway is 1.38 μs, and it is dominated almost entirely by Herzberg–Teller (HT) vibronic effects.

In water. During the analysis of the UV absorption spectra, it was already observed that the photochemical behavior differs between vacuum and polar environments. For example, the lowest-energy excited state localized on the benzopyran fragment corresponds to S_2 rather than S_3. In light of this, it is useful to examine separately how the relaxation behavior of the excited states is affected in water. Rather than analyzing all geometrical changes in detail, here we focus on the most relevant configurations, namely equilibrium geometries and conical intersections. Although the oscillator strength is slightly higher than in vacuum, the $S_0 \rightarrow S_1$ excitation remains weak and therefore unlikely in polar environment. If the SP system (Figure S15) is nevertheless excited to the S_1 state (Figure S16), the relaxation pathway resembles that observed in vacuum. In this case, the N—C bond connecting the NO_2 fragment to the pyran ring shortens from 1.455 Å (ground state) to 1.387 Å (excited state), whereas the N—O bonds elongate from 1.215 to 1.281 Å. The calculated fluorescence lifetime for this relaxation channel is 48 ns, which is about two orders of magnitude shorter than in vacuum. Here, the HT vibronic effects also dominate over the Frank–Condon contributions. In contrast, relaxation following the $S_0 \rightarrow S_2$ vertical excitation proceeds through the S_2–$R_e(S_1)^b$–$R_e(S_1)^c$–$R_e(S_1)^d$ channel (for BP fragment geometries and relative energies, see rows 20–23 in Table 2). During the relaxation step from $R_e(S_1)^b$ to $R_e(S_1)^c$, the C_2—C_3 bond is stretched, while the C_1—C_2 and C_3—C_4 bonds shorten as the system rotates around the C_2—C_3 axis. The energy decreases from 3.74 to 3.26 eV. In the subsequent step between $R_e(S_1)^c$ and $R_e(S_1)^d$, the fragment undergoes further rotation around C_2—C_3, and the C_1—O_6 bond is broken. The opening of the six-membered ring results in an additional energy decrease of 0.18 eV. The corresponding molecular structures of $ci(S_2 \times S_1)$, $R_e(S_1)^b$, TS^1, $R_e(S_1)^c$, TS^2, and $R_e(S_1)^d$ are presented in Figures S17–S22 of the Supporting Information. The essential difference between the vacuum and polar environmental cases is that, while the global minimum corresponds to the $R_e(S_1)^c$ conformation in vacuum, it becomes $R_e(S_1)^d$ in water. Thus, in the polar environment, the transition from the closed to the open configuration already occurs during relaxation. Accordingly, the light-induced conformational change appears to be more efficient in water, since it proceeds through an excited-state geometry that favors the MC form (Figure S23).

For the geometries associated with conical intersection points, the configurations obtained in vacuum were also reproduced in water using the same SF-TDDFT/ωB97X-D3BJ/def2-TZVPP level of theory. For the a-indexed, closed five-ring *ci* geometries (Figures S8, S24), the bond parameters of the 2*H*-pyran fragment are almost identical in vacuum and polar environments (see rows 9 and 25 in Table 2). However, more significant changes occur in the open, b-indexed *ci* geometry (Figure S25) of the 2*H*-pyran ring due to solvation. Although the bond length variations are moderate (see rows 10 and 26 in Table 2), the solvent significantly alters the character of the electronic states near the crossing geometry. In this case, rather than a typical two-state crossing, a third state becomes involved, leading to a nearly simultaneous three-state intersection. Specifically, a complex $T_2 \times S_0 \times S_1$ multiple crossing is formed, with the $T_2 - S_0$ and $S_0 - S_1$ energy gaps both being 0.00007 au (0.002 eV). A similar triple crossing has also been reported in pyrrole [44–46].

2.1.3 | Excited-State Relaxation: Indoline Channel

It is well established that both the benzopyran and indoline fragments can deform during excited-state relaxation [47]. Analysis of the NDO profiles shows that the S_5 excitation is mainly localized on the indoline fragment (see Table S1 in the Supporting Information). This localization suggests an indoline-centered relaxation pathway analogous to the benzopyran pathway. To investigate this, a geometry relaxation was initiated from the S_5 vertical excitation (242 nm, 5.12 eV), accounting for the possible "root flipping" effects in order to reach the lowest accessible excited state for the equilibrium geometry. During the optimization, the N_d—C_1 bond elongates considerably and then shortens again as the equilibrium is approached. The configuration corresponding to the maximum C_1—N_d bond is denoted $R_{int}(S_5)$, while the final equilibrium geometry is labeled $R_e(S_5)$. The relevant bond lengths and relative energies are listed in Table 3. Starting from the fifth excited state and allowing for "root flipping", the final equilibrium geometry corresponds to the first excited state, which coincides with $R_e(S_1)^c$. This result indicates that the relaxation channel initially associated with the indoline fragment ultimately transfers to the benzopyran fragment after some relaxation time. By following the energy profile along this relaxation channel, the intermediate configuration $R_{int}(S_5)$, corresponding to the longest N_d—C_1 bond, was selected for further analysis. At this geometry, the N_d—C_1 bond, initially 1.343 Å long, extends to 1.487 Å. From this point, a conical intersection search was performed to determine whether the *ci* configuration described in Ref. [47] could be reproduced. Indeed, such a *ci* geometry was found, in which the five-membered 2-pyrroline ring of the indoline fragment fully opens, and the N_d—C_1 bond length increases to 2.458 . It is also important to note that, based on the $R_e(S_1)^c$ equilibrium geometry, the probability of a direct transition from the S_1 state to the ground state via $ci(S_1 \times S_0)^c$ is low (Figure S26). This is because the open benzopyran fragment present in the $R_e(S_1)^c$ state must close, while the indoline fragment must simultaneously open. These two processes that can occur only during the early stages of S_5 relaxation, before the system reaches $R_{int}(S_5)$. Finally, when the transition to the S_0 ground state occurs through the conical intersection, the indoline five-membered ring recloses, restoring the SP conformation. It

TABLE 3 | The bond lengths (in Å) of the 2-pyrroline five-membered ring fragment for different equilibrium (R_e), intermediate (R_{int}), and conical intersection (*ci*) geometries, along with their relative energies (in eV), computed at the ωB97X-D3BJ/def2-TZVPP level of theory in vacuum. (For atomic indices, see Figure 1).

Bonds	Geometries			
	$R_e(S_0)$	$R_{int}(S_5)$	$R_e(S_5)$	$ci(S_1 \times S_0)^c$
C_1—C_a	1.561	1.586	1.613	1.500
C_a—C_b	1.508	1.490	1.492	1.521
C_b—C_c	1.391	1.412	1.399	1.442
C_c—N_d	1.396	1.341	1.363	1.306
N_d—C_1	1.343	1.487	1.434	2.458
En.	0.0	4.59	3.38	3.63

would also be worthwhile to investigate the role of the triplet manifold in this case, since the behavior of both the 2*H*-pyran and indoline rings becomes complex upon ring opening [48].

2.2 | MC to SP Conversion

The back transformation is at least as important as the light-induced conformational change discussed in the previous section. Accordingly, the equilibrium geometry and harmonic vibrational frequencies of the MC conformation were calculated at the same theoretical level as those of the SP. The nudged elastic band (NEB) method was employed to determine the minimum energy path (MEP) connecting the local minima corresponding to the reactant (SP) and product (MC) states on the potential energy surface. A total of eighteen intermediate images were generated between the SP and MC minima. The corresponding geometry changes in the most relevant fragment, the 2*H*-pyran six-membered ring, are listed in row 2 of Table 2. In vacuum, at the ground-state level, the conversion of MC to SP can be thermally activated via the transition state (TS) TS^3 (Figures S27 and S28), which has a barrier height of 0.76 eV. Although the absolute energy of TS^3 is slightly lower in water (1.39 eV) than in vacuum (1.53 eV), a higher barrier must be overcome for the system to switch from the MC to the SP conformation (1.04 eV in water vs. 0.76 eV in vacuum). The picture does not change significantly when another thermodynamic potential is considered instead of the electronic energy. Specifically, based on the Gibbs free energy derived from harmonic normal mode analysis, the barrier that must be overcome for the MC → SP conversion is 0.712 eV in vacuum and 1.001 eV in water. It is important to note that, although the number of intermediate images was increased in the NEB procedure to improve the resolution of the MEP, the resulting profile does not exhibit multiple peaks along the MC-SP back transformation. This finding contrasts, to some extent, with previous results on thermal back transformation, where multiple transition-state barriers were reported [36]. To obtain a more accurate description, the saddle-point geometry of TS^3 found using the NEB method was employed as the starting structure for subsequent calculations based on the intrinsic reaction coordinate (IRC) approach. The aim of this analysis was to determine the geometries of the endpoints, i.e., the SP and MC configurations, starting from the saddle point. Although a large number of iterations were required, the calculations show that the saddle point is directly connected to the endpoint geometries of SP and MC configurations. This result confirms that there are no multiple transition-state barriers and implicitly local minima between the SP and MC configurations. Of particular interest is the change in the C_2—C_3 bond length, which enables rotation around the bond axis. Near the saddle point, this bond is sufficiently elongated to allow such rotation (see Figures S31 and S32 in the Supporting Information). The Mayer's bond order index [49, 50] of C_2—C_3 bond in the TS^3 geometry configuration is 1.007 in vacuum and 0.998 in a polar environment.

2.2.1 | Absorption

The question arises of whether it is worthwhile to use light excitation to make the back transformation more efficient, and if so, how this could be achieved. Analogously to the SP case, the excitation energies of the MC conformation were determined at four different theoretical levels (see the definition of the M1 – M4 methods in the second paragraph of the section *Results and Discussion*). Consequently, the electronic excited-state energies and their oscillator strengths were computed using the ωB97X-D3BJ/def2-TZVPP hybrid and SOS-PBE-QIDH double-hybrid XC functionals, both in vacuum and polar environments. The results are summarized in Table S5 of the Supporting Information. First, based on absorption intensity, it can be concluded that the $S_0 \rightarrow S_1$ vertical, $\pi \rightarrow \pi^*$ type excitation is highly efficient across all four M1 – M4 computational schemes. The corresponding electronic transition is delocalized over nearly the entire molecule, involving the NO_2, 2*H*-pyran, pyrrole, and aromatic six-membered ring fragments. (See the NDO profiles reported in Tables S6-S9 of the Supporting Information.) Second, significant shifts in absorption energies arise from electron correlation effects, leading to a redshift of $\approx$80 nm in both vacuum and polar environments (from 399 to 481 nm in vacuum, and from 400 to 486 nm in water). Furthermore, the electronic excitations of the SP and MC conformations occur in different spectral regions (around 290 nm in vacuum and 300 nm in solvent for SP, versus $\approx$300 and 480 nm for MC). This implies that the two conformations can be selectively excited. Finally, the solvent environment has little influence on the $S_0 \rightarrow S_1$ transition, while its effect becomes more pronounced for the second and higher excited states (see Table S5 in the Supporting Information).

2.2.2 | Excited-State Relaxation

The relaxation of the excited electronic state naturally begins on the potential energy surface (PES) of S_1.

In vacuum. The system first reaches the local minimum $R_e(S_1)^d$ (Figure S29), crosses the TS^2 saddle point (Figure S30) with an energy barrier of 0.06 eV, and finally arrives at the global equilibrium geometry $R_e(S_1)^c$. From this geometry, relaxation proceeds toward the S_0 ground state as described in the previous subsection. In this process, several relaxation pathways can occur. One possible route involves radiative decay, where the system relaxes from the global S_1 minimum to the S_0 state via fluorescence, and further relaxation along the S_0 PES yields the SP conformation. Alternatively, the system can undergo nonradiative transitions: in one case, radiationless decay proceeds through the $ci(S_1 \times S_0)^a$ conical intersection, followed by relaxation to the $R_e(S_0)^{SP}$ geometry, while in another, the decay takes place via the $ci(S_1 \times S_0)^b$ intersection, leading to the $R_e(S_0)^{MC}$ geometry. Among these pathways, two result in the conversion from MC to SP, while the remaining one retains the MC conformation.

In water. Following the $S_0 \rightarrow S_1$ excitation, the global minimum on the S_1 surface corresponds to the $R_e(S_1)^d$ geometry, rather than $R_e(S_1)^c$. As a consequence, after either radiative (fluorescence-type) or nonradiative decay, the system is unlikely to adopt the SP conformation and instead remains in the MC form. This occurs because, starting from both the $R_e(S_1)^d$ and $ci(S_1 \times S_0)^b$ geometries, subsequent relaxation on the S_0 PES leads directly back to the MC configuration.

2.3 | Relaxation in the Triplet Manifold

In many cases, pathways that initially proceed along a singlet potential energy surface can undergo an intersystem crossing (ISC) to a triplet state, allowing excited-state relaxation to continue on the triplet manifold [36, 51–53]. This phenomenon involving triplet spin states has also been experimentally observed for SP, where relaxation of the excited states results in phosphorescent emission [54]. Consequently, the energies of the triplet ground and excited states were calculated for the $R_e(S_1)^a$, $R_e(S_1)^c$, and $R_e(S_1)^d$ geometries in both vacuum and polar environments. In addition, geometry optimizations were carried out for the triplet ground (T_1) and first excited (T_2) states, followed by normal-mode vibrational analyses for each optimized structure. Figure 6 shows the energy diagrams of the singlet and triplet electronic states for the $R_e(S_1)^a$, $R_e(S_1)^c$, and $R_e(S_1)^d$ geometries, as well as for the optimized $R_e(T_1)$ and $R_e(T_2)$ triplet states in vacuum. Figure 7 presents the corresponding diagrams for the polar environment. For the $R_e(S_1)^a$ geometry in vacuum, the triplet ground state (T_1) is 0.17 eV below the first singlet excited state S_1 state, whereas the first triplet excited state (T_2) is located 0.66 eV above it. Geometry optimization process converges only for the T_1 state; attempts to optimize the T_2 state result in relaxation to T_1, yielding an equilibrium geometry identical to $R_e(T_1)$. The optimized T_1 geometry closely resembles $R_e(S_0)$, with differences only in the internal coordinates of the NO_2 fragment. The polar environment slightly modifies the triplet energy levels but does not significantly affect the overall energetic ordering for the $(S_1)^a$ case. The corresponding bond lengths and relative energies for the 2*H*-pyran fragment are listed in Table 4, and the molecular structures are shown in Figures S33–S42 of the Supporting Information. For the $R_e(S_1)^c$ geometry (shown in gray in Figure 6), the T_1 and T_2 states are more separated in energy from the singlet. Specifically, T_1 is 0.17 eV below $(S_1)^c$, while T_2 is 0.5 eV above it. Geometry optimization of both T_1 and T_2 shows similar behavior to the $(S_1)^a$ case, except that in this case a local minimum was also found for T_2. Nevertheless, optimization initiated from the $(S_1)^c$ geometry again leads to relaxation from T_2 to T_1. The calculated ISC rate between S_1 and T_1 was nearly zero, indicating that the singlet-triplet transition is unlikely. In aqueous environment, however, both T_1 and T_2 equilibrium geometries were successfully located, enabling a more efficient singlet-triplet conversion. Indeed, the ISC rate (k_{isc}) calculated for the $S_1 \times T_2$ spin transition is $2.962 \cdot 10^9\ s^{-1}$. For the $(S_1)^d$ geometry, the T_2 triplet lies 0.1 eV below the singlet in vacuum and 0.43 eV above it in water. After energy relaxation, T_2 becomes 0.44 eV lower in vacuum, while nearly identical energy levels are obtained in polar environment. Overall, the singlet–triplet transition appears to be an efficient process in both environments, with the aqueous medium promoting faster spin conversion. The ISC rate can be up to an order of magnitude higher in water ($3.396 \cdot 10^9\ s^{-1}$) than in vacuum ($3.238 \cdot 10^{10}\ s^{-1}$), suggesting that the polar environment favors the spin transition.

In general, for open MC-type geometries, the transition from the first excited singlet S_1 to the first excited triplet T_2 is much more probable, and this likelihood is further enhanced in an aqueous environment. Similar conclusions have been reported in experimental studies [55–57], though a more detailed analysis would be necessary to fully understand the relaxation mechanisms on the triplet manifold, which should include nonradiative and radiative transitions between different triplet states, back transformations from triplet to singlet states, or even the SP ⇌ MC interconversion at triplet electronic states. And, of course, all of these analyses should be performed in different solvent environments.

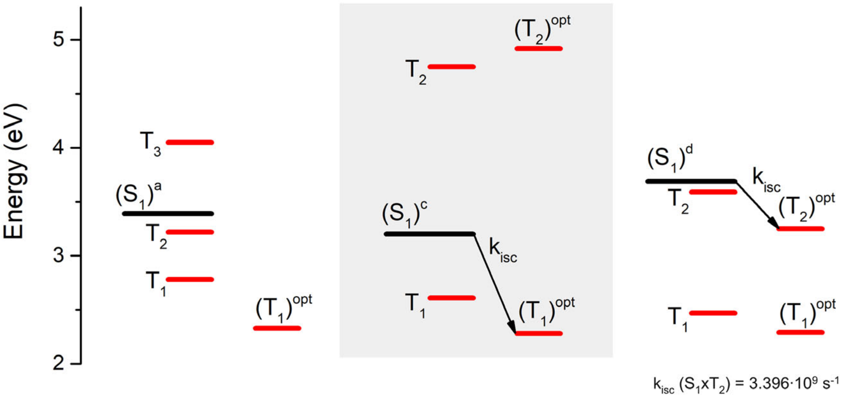

FIGURE 6 | The energy diagram of the singlet and triplet electronic states computed at the DFT and TDDFT/ωB97X-D3BJ/def2-TZVPP levels of theory in vacuum.

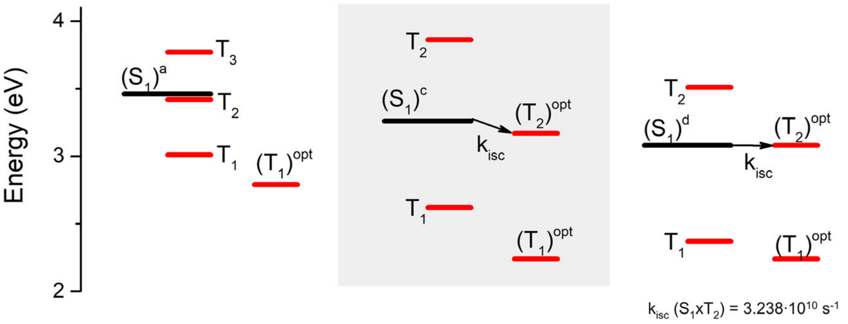

FIGURE 7 | The energy diagram of the singlet and triplet electronic states computed at the DFT and TDDFT/ωB97X-D3BJ/def2-TZVPP levels of theory in polar environment.

TABLE 4 | The bond lengths (in Å) of the 2*H*-pyran six-membered ring fragment for different triplet equilibrium (R_e) geometries along with their relative energies (in eV) computed at the ωB97X-D3BJ/def2-TZVPP level of theory in both vacuum and polar environments.

Nr.	Geom.	C_1—C_2	C_2—C_3	C_3—C_4	C_4—C_5	C_5—O_6	C_1—O_6	C_2—O_6	En.
2*H*-pyran fragment in SP and MC in vacuum									
1	$R_e(S_0)^{SP}$	1.496	1.325	1.455	1.397	1.340	1.455	—	0.00
2	$R_e(S_0)^{MC}$	1.375	1.395	1.384	1.474	1.230	—	2.837	0.77
3	$R_e(T_1)^a$	1.497	1.326	1.455	1.395	1.347	1.450	2.431	2.33
4	$R_e(T_1)^c$	1.469	1.493	1.391	1.419	1.334	2.447	1.493	2.28
5	$R_e(T_1)^d$	1.387	1.378	1.447	1.475	1.240	—	2.891	4.92
6	$R_e(T_2)^c$	1.467	1.486	1.346	1.459	1.320	2.455	1.486	2.29
7	$R_e(T_2)^d$	1.376	1.389	1.434	1.415	1.323	—	2.769	3.25
2*H*-pyran fragment in SP and MC in water									
8	$R_e(S_0)^{SP}$	1.495	1.325	1.456	1.398	1.338	1.460	—	0.00
9	$R_e(S_0)^{MC}$	1.410	1.363	1.423	1.457	1.247	—	2.868	0.35
10	$R_e(T_1)^a$	1.496	1.326	1.456	1.397	1.346	1.455	2.435	2.79
11	$R_e(T_1)^c$	1.384	1.458	1.397	1.460	1.261	2.994	2.410	2.24
12	$R_e(T_1)^d$	1.389	1.381	1.444	1.474	1.243	—	2.910	2.24
13	$R_e(T_2)^c$	1.397	1.430	1.413	1.444	1.267	2.840	2.399	3.17
14	$R_e(T_2)^d$	1.386	1.400	1.407	1.486	1.237	—	2.815	3.08

2.4 | Summary of Relaxation Channels

The different pathways of the SP ⇌ MC interconversion defined by radiative or radiationless deactivation processes are shown in Figure 8 for vacuum and in Figure 9 for aqueous environments. The black, red, and magenta colors in these two figures were chosen to indicate the individual relaxation channels. The vertical arrows on the left and right sides of the figure represent vertical electronic excitations. Short horizontal lines are used to indicate various relevant geometries, such as equilibrium, a saddle point, or a conical intersection. With sloping arrows connecting different geometries, the assumed relaxation paths and their possible directions are indicated. The question arises, of course, as to whether the results can be plotted on the same graph given the different reference methods employed (restricted versus unrestricted in the case of TDDFT, and spin-flipped TDDFT). Ground state calculations for the *ci* geometries demonstrate that the difference in energies can only be observed in the fifth decimal place due to the different reference methods.

2.4.1 | SP to MC Conversion

Channel 1 (black path):This pathway begins with the $S_0 \rightarrow S_1$ vertical excitation of the SP molecule, followed by relaxation to the $R_e(S_1)^a$ equilibrium geometry. From this excited-state geometry, two deactivation pathways are possible. In the first, the molecule

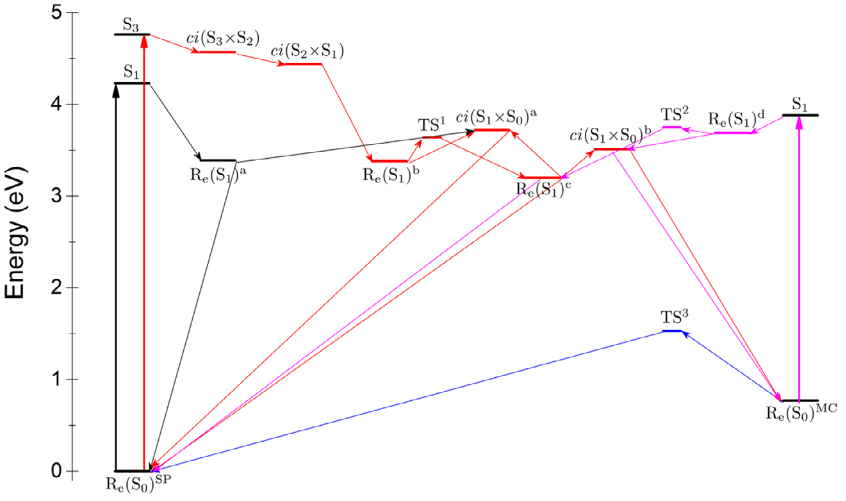

FIGURE 8 | The SP–MC interconversion scheme including the most relevant ground and electronic excited state $R_e(S_i)$, $i = 0, 1, 2, 3$, conical intersection $ci(S_i \times S_j)$ and TS geometries along the different relaxation channels in vacuum environment.

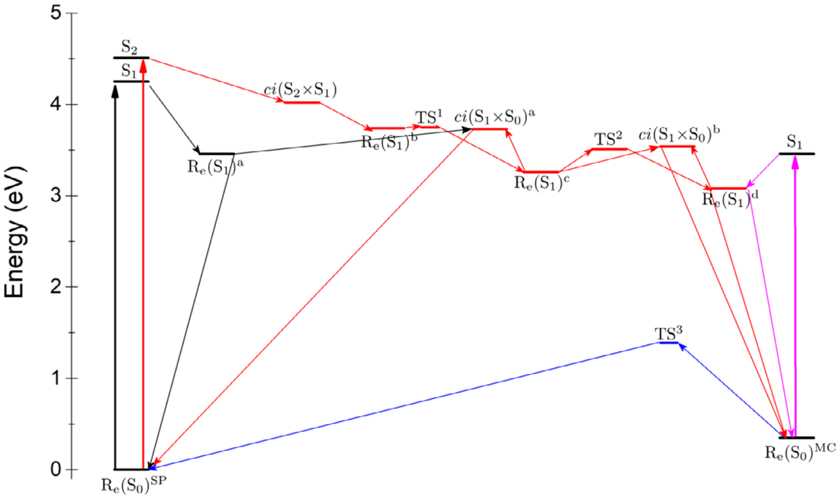

FIGURE 9 | The SP–MC interconversion scheme including the most relevant ground and electronic excited state $R_e(S_i)$, $i = 0, 1, 2, 3$, conical intersection $ci(S_i \times S_j)$ and TS geometries along the different relaxation channels in aqueous environment.

decays radiatively via fluorescence to the $R_e(S_0)^{SP}$ ground-state geometry. In the second, a radiationless transition occurs through the $ci(S_1 \times S_0)^a$ conical intersection, leading to the same $R_e(S_0)^{SP}$ configuration.

Channel 2 (red path):*i*) In vacuum. Following the $S_0 \rightarrow S_3$ vertical excitation, relaxation proceeds through the $ci(S_3 \times S_2)$ and subsequently the $ci(S_2 \times S_1)$ conical intersections. Thus, the system rapidly decays from S_3 to S_1, reaching the local minimum $R_e(S_1)^b$ on the potential energy surface. Passing over the TS^1 saddle point, the system reaches the global minimum $R_e(S_1)^c$ on the S_1 surface. From here, three deactivation channels are possible: **2a** – radiative decay via fluorescence to $R_e(S_0)^{SP}$; **2b** – radiationless transition through the $ci(S_1 \times S_0)^a$ point, also yielding $R_e(S_0)^{SP}$; and **2c** – radiationless transition through the $ci(S_1 \times S_0)^b$ point, leading to $R_e(S_0)^{MC}$. *ii*) In water. In the aqueous environment, the pathway starts with the $S_0 \rightarrow S_2$ vertical excitation, followed by relaxation to $R_e(S_1)^b$ via the $ci(S_2 \times S_1)$ conical intersection. Subsequently, the system crosses the TS^1 TS to reach $R_e(S_1)^c$, then passes the TS^2 TS to arrive at the global minimum $R_e(S_1)^d$. From this geometry, the SP system decays either radiatively through florescence or nonradiatively via the $ci(S_1 \times S_0)^b$ conical intersection, both processes leading to the $R_e(S_0)^{MC}$ geometry.

2.4.2 | MC to SP Conversion

Channel 1 (blue path):The conformational transition from MC to SP can occur, without the involvement of excited states. In this case, the MC system must overcome an energy barrier of 0.76 eV in a vacuum and 1.04 eV in aqueous environment.

Channel 2 (magenta path):The efficiency of the light-induced back transformation depends strongly on the environment, namely, whether the system is in vacuum or in solution. In vacuum, $S_0 \rightarrow S_1$ vertical excitation of the MC geometry first relaxes to the local minimum $R_e(S_1)^d$, then to the global minimum $R_e(S_1)^c$. This latter configuration is favorable for SP-like structural rearrangements, since both radiative and nonradiative relaxation through the $ci(S_1 \times S_0)^a$ point lead to SP geometries. However, nonradiative decay via the $ci(S_1 \times S_0)^b$ intersection can also return the system to the original MC structure. In water, the global minimum corresponds to the $R_e(S_1)^d$ geometry, which is close to the open form of the 2*H*-pyran fragment. Therefore, it is highly unlikely that radiative or nonradiative relaxation from this state would result in the SP conformation.

3 | Conclusion

The complete photochromic transformation process between SP and MC was investigated using DFT, linear-response TDDFT, and spin-flip TDDFT methods. Calculations employed the *ω*B97X-D3BJ exchange-correlation functional with empirical dispersion corrections, the CPCM for solvation, and the def2-TZVPP triple-*ζ* basis set. The most relevant molecular configurations, equilibrium, transition-state, and conical-intersection geometries, were mapped, and the energetically most favorable relaxation pathways were identified. In the SP → MC conversion, these relaxation channels originate from at least the second electronic excited state, which subsequently passes through one or two conical intersections before reaching the first excited state. Along the potential energy surface of the first excited state, additional barriers are overcome until the system reaches its global minimum. From there, the system returns to the ground state, either radiatively or nonradiatively. Depending on the geometry of this S_1 minimum, the system either retains the original SP form or transforms into the open MC configuration. These results reveal a highly complex photochemical behavior, in which not only the excitation energies but also the surrounding environment play a decisive role. In vacuum, relaxation from the excited states can convert SP to MC only through one of the conical intersection points and only nonradiatively. In contrast, in an aqueous environment, both radiative and nonradiative transitions can lead to the MC form. This difference arises because the geometry of the global minimum on the first excited-state surface differs in vacuum and in water. Conversely, the thermal back transformation from MC to SP must overcome a relatively high potential barrier, resulting in long-term stability of the open MC configuration. In addition, combined "NEB + IRC" calculations prove that the process of the thermal reconversion occurs at the ground state level does not exhibit multiple barriers and implicitly local minima along the transformation path between the SP and

MC conformations. On the other hand, light-induced back conversion is more efficient in vacuum than in aqueous environment, again due to differences in the equilibrium geometry of the first excited singlet states. Furthermore, relaxation along the triplet manifold may also be a possible component of the relaxation pathway; results concerning the ISC rate indicate that a rapid singlet-triplet spin transition may occur starting from the first excited singlet states associated with the open geometry conformation.

4 | Computational Details

Ground-state equilibrium geometries and vibrational normal-mode frequencies were obtained within the framework of the density functional theory (DFT) using the ωB97X-D3BJ exchange-correlation (XC) functional [58, 59], which includes Grimme’s D3-type empirical dispersion correction scheme [60, 61]. The def2-TZVPP triple-ζ basis set of the Karlsruhe group [62] was employed as implemented in the ORCA program suite [63, 64]. Excited-state equilibrium geometries were computed using the linear-response time-dependent DFT (LR-TDDFT) [65, 66], while the conical intersection (*ci*) geometries were obtained using the spin-flip time-dependent DFT (SF-TDDFT) [43, 67–71] method implemented in the same software package. To accelerate hybrid DFT calculations, the RIJCOSX approximation [72–77] was applied together with the def2/J [78] auxiliary basis set for Coulomb fitting. In the LR-TDDFT calculations, the Tamm–Dancoff approximation [79] and the def2-TZVPP/C [80] auxiliary basis set for correlation fitting were also employed. The electronic excited-state energies were further refined using the SOS-PBE-QIDH [81] double-hybrid XC functional. For the *ci* geometries obtained via SF-TDDFT, excited-state energies were also computed with the multireference complete active space SCF (or CASSCF) method and the fully internally contracted *n*-electron valence state perturbation theory (FIC-NEVPT2) [82]. which use the CASSCF-type reference wave functions. TS geometries and MEPs connecting equilibrium and conical-intersection structures on different electronic-state potential energy surfaces were located using the NEB method [83, 84]. IRC method [85] was used to confirm that a proposed TS correctly connects the intended reactants and products. Solvent effects were modeled using the CPCM [86, 87]. Theoretical predictions on fluorescence and phosphorescence rates were obtained using the path-integral approach to excited-state dynamics, by solving Fermi’s Golden Rule-type equations including vibronic coupling for formally forbidden transitions (the HT effect) and Duschinsky rotations between normal modes of different electronic states [88–90]. The molecular geometries were built, analyzed, and manipulated using Gabedit [91] and Avogadro [92] and the molecular graphics were prepared with GaussView [93].

Acknowledgments

This work was supported by the Romanian Ministry of Research, Innovation, and Digitization (MCID) through the “Nucleu” Program within the National Plan for Research, Development and Innovation 2022–2027, project code PN 23 24 01 02. The authors also thank INCDTIM, Cluj-Napoca Data Center, for providing computer facilities supported through the POC project “The development of the INCDTIM DATA CENTER for the creation of a CLOUD platform, integrated in European CDI networks” no. 348/390024/08.09.2021. Zs. B. gratefully acknowledges the support of the Collegium Talentum Program of Hungary.

Funding

This study was supported by Romanian Ministry of Education and Research (PN 23 24 01 02).

Conflicts of Interest

The authors declare no conflicts of interest.

References

1. J. K. Rad, Z. Balzade, and A. R. Mahdavian, “Spiropyran-Based Advanced Photoswitchable Materials: A Fascinating Pathway to the Future Stimuli-Responsive Devices,” *Journal of Photochemistry and Photobiology C: Photochemistry* 51 (2022): 100487.

2. G. Berkovic, V. Krongauz, and V. Weiss, “Spiropyrans and Spirooxazines for Memories and Switches,” *Chemical Reviews* 100 (2000): 1741–1753.

3. M.-M. Russew and S. Hecht, “Photoswitches: From Molecules to Materials,” *Advanced Materials* 22 (2010): 3348–3360.

4. M. Irie, T. Fukaminato, K. Matsuda, and S. Kobatake, “Photochromism of Diarylethene Molecules and Crystals: Memories, Switches, and Actuators,” *Chemical Reviews* 114 (2014): 12174–12277.

5. A. J. McConnell, C. S. Wood, P. P. Neelakandan, and J. R. Nitschke, “Stimuli-Responsive Metal - Ligand Assemblies,” *Chemical Reviews* 115 (2015): 7729–7793.

6. J. Orrego-Hernández, A. Dreos, and K. Moth-Poulsen, “Engineering of Norbornadiene/Quadricyclane Photoswitches for Molecular Solar Thermal Energy Storage Applications,” *Accounts of Chemical Research* 53 (2020): 1478–1487.

7. M. J. Fuchter, “On the Promise of Photopharmacology Using Photoswitches: A Medicinal Chemist’s Perspective,” *Journal of Medicinal Chemistry* 63 (2020): 11436–11447.

8. V. M. Lechner, M. Nappi, P. J. Deneny, S. Folliet, J. C. K. Chu, and M. J. Gaunt, “Visible-Light-Mediated Modification and Manipulation of Biomacromolecules,” *Chemical Reviews* 122 (2022): 1752–1829.

9. X. Wang, B. Xu, and W. Tian, “Solid-State Luminescent Molecular Photoswitches,” *Accounts of Materials Research* 4 (2023): 311–322.

10. K. Imato, N. Kaneda, and Y. Ooyama, “Recent Progress in Photoinduced Transitions between the Solid, Glass, and Liquid States based on Molecular Photoswitches,” *Polymer Journal* 56 (2024): 269–282.

11. L. Kortekaas and W. R. Browne, “The Evolution of Spiropyran: Fundamentals and Progress of an Extraordinarily Versatile Photochrome,” *Chemical Society Reviews* 48 (2019): 3406–3424.

12. B. L. Feringa, R. A. van Delden, N. Koumura, and E. M. Geertsema, “Chiroptical Molecular Switches,” *Chemical Reviews* 100 (2000): 1789–1816.

13. J. Buback, M. Kullmann, F. Langhojer, et al., “Ultrafast Bidirectional Photoswitching of a Spiropyran,” *Journal of the American Chemical Society* 132 (2010): 16510–16519.

14. M. Mostaghimi, H. P. Hernandez, Y. Jiang, W. Wenzel, L. Heinke, and M. Kozlowska, “On - Off Conduction Photoswitching in Modelled Spiropyran-based Metal-Organic Frameworks,” *Communications Chemistry* 6 (2023): 275.

15. D. S. Achilleos, T. A. Hatton, and M. Vamvakaki, “Light-Regulated Supramolecular Engineering of Polymeric Nanocapsules,” *Journal of the American Chemical Society* 134 (2012): 5726–5729.

16. R. Q. Albuquerque, J. Kühni, P. Belser, and L. D. Cola, “On the Reversible Photoisomerization of Spiropyran-Modified Zeolite L Single Crystals,” *ChemPhysChem* 11 (2010): 575–578.

17. A. S. Kozlenko, I. V. Ozhogin, A. D. Pugachev, M. B. Lukyanova, I. M. El-Sewify, and B. S. Lukyanov, “A Modern Look at Spiropyrans: From Single Molecules to Smart Materials,” *Topics in Current Chemistry* 381 (2023): 8.

18. B. Zhou, A. Govyadinov, P. Kornilovitch, and V. T. Remcho, “Development of Spiropyran Immobilization and Characterization Protocols for Reversible Photopatterning of SiO_2 Surfaces,” *ACS Omega* 9 (2024): 29401–29409.

19. R. Klajn, “Spiropyran-based dynamic materials,” *Chemical Society Reviews* 43 (2014): 148–184.

20. S. Ding, X. Lv, Y. Xia, and Y. Liu, “Fluorescent Materials Based on Spiropyran for Advanced Anti-Counterfeiting and Information Encryption,” *Molecules* 29 (2024): 2536.

21. X. Wang, H. Yu, R. Yang, et al., “Fluorescence Switching and Photoisomerization of a Spiropyran Molecular Photoswitch through Confined Spaces Regulation in Crystals,” *The Journal of Physical Chemistry Letters* 15 (2024): 4224–4228.

22. J. Bonefacino, M.-L. V. Tse, C.-F. J. Pun, et al., “Characterization of Spirooxazine and Spiropyran Hosted in Poly(Methyl Methacrylate) for Germicidal UV Source,” *Optics and Photonics Journal* 3 (2013): 11–16.

23. A. Fagan, M. Bartkowski, and S. Giordani, “Spiropyran-Based Drug Delivery Systems,” *Frontiers in Chemistry* 9 (2021): 720087.

24. J. Piard, “Influence of the Solvent on the Thermal Back Reaction of One Spiropyran,” *Journal of Chemical Education* 91 (2014): 2105–2111.

25. A.-K. Holm, M. Rini, E. T. J. Nibbering, and H. Fidder, “Femtosecond UV/mid-IR study of Photochromism of the Spiropyran 1 0,3 0-dihydro-1 0,3 0,3 0-trimethyl-6-nitrospiro- [2H-1-benzopyran-2,2 0-(2H)-indole] in Solution,” *Chemical Physics Letters* 376 (2003): 214–219.

26. J. Hobley, U. Pfeifer-Fukumura, M. Bletz, T. Asahi, H. Masuhara, and H. Fukumura, “Ultrafast Photo-Dynamics of a Reversible Photochromic Spiropyran,” *The Journal of Physical Chemistry. A* 106 (2002): 2265–2270.

27. M. Hammarson, J. R. Nilsson, S. Li, T. Beke-Somfai, and J. Andreasson, “Characterization of the Thermal and Photoinduced Reactions of Photochromic Spiropyrans in Aqueous Solution,” *The Journal of Physical Chemistry. B* 117 (2013): 13561–13571.

28. W. Tian and J. Tian, “Synergy of Different Fluorescent Enhancement Effects on Spiropyran Appended onto Cellulose,” *Langmuir* 30 (2014): 3223–3227.

29. C. Özçoban, T. Halbritter, S. Steinwand, et al., “Water-Soluble Py-BIPS Spiropyrans as Photoswitches for Biological Applications,” *Organic Letters* 17 (2015): 1517–1520.

30. K. A. Palasis and A. D. Abell, “Effect of Indoline Substitution on Ring Opening in 6-nitro BIPS Spiropyran Derivatives,” *Tetrahedron Letters* 138 (2024): 154967.

31. P. Celani, F. Bernardi, M. Olivucci, and M. A. Robb, “Conical Intersection Mechanism for Photochemical Ring Opening in Benzospiropyran Compounds,” *Journal of the American Chemical Society* 119 (1997): 10815–10820.

32. I. Gómez, M. Reguero, and M. A. Robb, “Efficient Photochemical Merocyanine-to-Spiropyran Ring Closure Mechanism through an Extended Conical Intersection Seam. A Model CASSCF/CASPT2 Study,” *The Journal of Physical Chemistry. A* 110 (2006): 3986–3991.

33. F. Liu and K. Morokuma, “Multiple Pathways for the Primary Step of the Spiropyran Photochromic Reaction: A CASPT2//CASSCF Study,” *Journal of the American Chemical Society* 135 (2013): 10693–10702.

34. S. Prager, I. Burghardt, and A. Dreuw, “Ultrafast C_{Spiro} - O Dissociation via a Conical Intersection Drives Spiropyran to Merocyanine Photoswitching,” *The Journal of Physical Chemistry. A* 118 (2014): 1339–1349.

35. H. Roohi and T. Rostami, “Mechanism of the Photo Triggered Ring-Opening Reaction of Spiropyran Derivatives (SP-X1-7; X1-7 = H, NO_2, CF_3, CN, OH, OMe and NMe_2) in the Gas Phase and Various Solvent Media: A GD3-TD-DFT Approach,” *Journal of Photochemistry and Photobiology. A, Chemistry* 392 (2020): 112410.

36. Y. Sheng, J. Leszczynski, A. A. Garcia, R. Rosario, D. Gust, and J. Springer, “Comprehensive Theoretical Study of the Conversion Reactions of Spiropyrans: Substituent and Solvent Effects,” *The Journal of Physical Chemistry. B* 108 (2004): 16233–16243.

37. G. Granucci and G. Padula, “Photoisomerization Dynamics of Spiropyran: A Surface-Hopping Investigation,” *The Journal of Chemical Physics* 154 (2021): 124312.

38. I. N. Dobrovolskiy and V. V. Kostjukov, “TD-DFT study of BIPS spiropyran: Effects of functionals and High-Polarity Solvent on C—O bond Dissociation and Recovery,” *Journal of Computational Chemistry* 44 (2023): 1928–1940.

39. V. V. Kostjukov, “TD-DFT Analysis of Excitation of the Closed-Form Spironaphthopyran in Methanol Solution: The Contribution of Vibronic Transitions and Intermolecular Hydrogen Bonds,” *Journal of Molecular Graphics & Modelling* 128 (2024): 108705.

40. J. M. Herbert, X. Zhang, A. F. Morrison, and J. Liu, “Beyond Time-Dependent Density Functional Theory Using Only Single Excitations: Methods for Computational Studies of Excited States in Complex Systems,” *Accounts of Chemical Research* 49 (2016): 931–941.

41. J. M. Herbert, “Visualizing and Characterizing Excited States from Time-Dependent Density Functional Theory,” *Physical Chemistry Chemical Physics* 26 (2024): 3755–3794.

42. A. A. Khodonov, N. E. Belikov, A. Y. Lukin, et al., “5’-Substituted Indoline Spiropyrans: Synthesis and Applications,” *Colorants* 2 (2023): 264–404.

43. D. Casanova and A. I. Krylov, “Spin-Flip Methods in Quantum Chemistry,” *Physical Chemistry Chemical Physics* 22 (2020): 4326–4342.

44. S. Cogan, Y. Haas, and S. Zilberg, “Intersystem Crossing at Singlet Conical Intersections,” *Journal of Photochemistry and Photobiology. A, Chemistry* 190 (2007): 200–206.

45. L. Shen, B. Xie, Z. Li, L. Liu, G. Cui, and W.-H. Fang, “Role of Multistate Intersections in Photochemistry,” *The Journal of Physical Chemistry Letters* 11 (2020): 8490–8501.

46. Y. S. Baek, S. Lee, M. Filatov, and C. H. Choi, “Optimization of Three State Conical Intersections by Adaptive Penalty Function Algorithm in Connection with the Mixed-Reference Spin-Flip Time-Dependent Density Functional Theory Method (MRSF-TDDFT),” *The Journal of Physical Chemistry. A* 125 (2021): 1994–2006.

47. L. Fransén, B. Roux, S. Coriani, S. Nandi, and M. Vacher, “Tracking Photophysical Relaxation in Spiropyran with Simulated Time-Resolved X-Ray Absorption Spectroscopy,” *Communications Physics* 8 (2025): 263.

48. L. Poisson, K. D. Raffael, B. Soep, J.-M. Mestdagh, and G. Buntinx, “Gas-Phase Dynamics of Spiropyran and Spirooxazine Molecules,” *Journal of the American Chemical Society* 128 (2006): 3169–3178.

49. I. Mayer, “Charge, Bond Order and Valence in the AB Initio SCF Theory,” *Chemical Physics Letters* 97 (1983): 270.

50. I. Mayer, “Bond Order and Valence: Relations to Mulliken’s Population Analysis,” *International Journal of Quantum Chemistry* 26 (1984): 151–154.

51. C. M. Marian, “Understanding and Controlling Intersystem Crossing in Molecules,” *Annual Review of Physical Chemistry* 72 (2021): 617–640.

52. J. S. Zugazagoitia, E. Collado-Fregoso, E. F. Plaza-Medina, and J. Peon, “Relaxation in the Triplet Manifold of 1-Nitronaphthalene Observed by Transient Absorption Spectroscopy,” *The Journal of Physical Chemistry. A* 113 (2009): 805–810.

53. N. A. Lau, D. Ghosh, S. Bourne-Worster, et al., “Unraveling the Ultrafast Photochemical Dynamics of Nitrobenzene in Aqueous Solution,” *Journal of the American Chemical Society* 146 (2024): 10407–10417.

54. S. P. Naughton, R. M. Gaudet, A. A. Leslie, and A. E. Keirstead, “Direct Observation of Spiropyran Phosphorescence in Imidazolium Ionic Liquids,” *Chemical Physics Letters* 556 (2013): 102–107.

55. A. K. Chibisov and H. Görner, “Photoprocesses in Spiropyran-Derived Merocyanines,” *The Journal of Physical Chemistry. A* 101 (1997): 4305–4312.

56. A. Seret, M. Hoebeke, and A. Van de Vorst, “Triplet Yield of Merocyanine 540 in Water is Wavelength Dependent,” *Photochemistry and Photobiology* 52 (1990): 601–604.

57. H. Görner, “Photoprocesses in Spiropyrans and their Merocyanine Isomers: Effects of Temperature and Viscosity,” *Chemical Physics* 222 (1997): 315–329.

58. J.-D. Chai and M. Head-Gordon, “Long-Range Corrected Hybrid Density Functionals with Damped Atom-Atom Dispersion Corrections,” *Physical Chemistry Chemical Physics* 10 (2008): 6615.

59. S. Lehtola, C. Steigemann, M. Oliveira, and M. Marques, “Recent Developments in Libxc - A Comprehensive Library of Functionals for Density Functional Theory,” *Software X* 7 (2018): 1–5.

60. S. Grimme, J. Antony, S. Ehrlich, and H. Krieg, “A Consistent and Accurate Ab Initio Parametrization of Density Functional Dispersion Correction (DFT-D) for the 94 Elements H-Pu,” *The Journal of Chemical Physics* 132 (2010): 154104.

61. S. Grimme, S. Ehrlich, and L. Goerigk, “Effect of the Damping Function in Dispersion Corrected Density Functional Theory,” *Journal of Computational Chemistry* 32 (2011): 1456–1465.

62. F. Weigend and R. Ahlrichs, “Balanced Basis Sets of Split Valence, Triple Zeta Valence and Quadruple Zeta Valence Quality for H to Rn: Design and Assessment of Accuracy,” *Physical Chemistry Chemical Physics* 7 (2005): 3297–3305.

63. F. Neese, “Software Update: The ORCA Program System–Version 5.0,” *WIREs Computational Molecular Science* 12 (2022): e1606.

64. F. Neese, F. Wennmohs, U. Becker, and C. Riplinger, “The ORCA Quantum Chemistry Program Package,” *The Journal of Chemical Physics* 152 (2020): 224108.

65. E. Runge and E. K. U. Gross, “Density-Functional Theory for Time-Dependent Systems,” *Physical Review Letters* 52 (1984): 997–1000.

66. F. Neese and G. Olbrich, “Efficient Use of the Resolution of the Identity Approximation in Time-Dependent Density Functional Calculations with Hybrid Density Functionals,” *Chemical Physics Letters* 362 (2002): 170–178.

67. Z. Rinkevicius, O. Vahtras, and H. Ågren, “Spin-Flip Time Dependent Density Functional Theory Applied to Excited States with Single, Double, or Mixed Electron Excitation Character,” *The Journal of Chemical Physics* 133 (2010): 114104.

68. Y. Mei and W. Yang, “Excited-State Potential Energy Surfaces, Conical Intersections, and Analytical Gradients from Ground-State Density Functional Theory,” *The Journal of Physical Chemistry Letters* 10 (2019): 2538–2545.

69. S. Matsika, “Electronic Structure Methods for the Description of Nonadiabatic Effects and Conical Intersections,” *Chemical Reviews* 121 (2021): 9407–9449.

70. A. Bende, A.-A. Farcaş, A. Falamaş, and A. Petran, “New Insight into Catechol Photochemistry: The Role of Different Monomer and Dimer Configurations in Radiation-Less Decay of the S_1 lectronic Excited State,” *Physical Chemistry Chemical Physics* 24 (2022): 29165–29175.

71. A. Bende and A.-A. Farcaş, “Intermolecular-Type Conical Intersections in Benzene Dimer,” *International Journal of Molecular Sciences* 24 (2023): 2906.

72. F. Neese, “An Improvement of the Resolution of the Identity Approximation for the Formation of the Coulomb Matrix,” *Journal of Computational Chemistry* 24 (2003): 1740–1747.

73. F. Neese, F. Wennmohs, A. Hansen, and U. Becker, “Efficient, Approximate and Parallel Hartree-Fock and Hybrid DFT calculations. A ‘Chain-of-Spheres’ Algorithm for the Hartree-Fock Exchange,” *Chemical Physics* 356 (2009): 98–109.

74. R. Izsák and F. Neese, “An Overlap Fitted Chain of Spheres Exchange Method,” *The Journal of Chemical Physics* 135 (2011): 144105.

75. R. Izsák, F. Neese, and W. Klopper, “Robust Fitting Techniques in the Chain of Spheres Approximation to the Fock Exchange: The Role of the Complementary Space,” *The Journal of Chemical Physics* 139 (2013): 094111.

76. B. Helmich-Paris, B. de Souza, F. Neese, and R. Izsák, “An Improved Chain of Spheres for Exchange Algorithm,” *The Journal of Chemical Physics* 155 (2021): 104109.

77. F. Neese, “The SHARK Integral Generation and Digestion System,” *Journal of Computational Chemistry* 44 (2022): 381–396.

78. F. Weigend, “Accurate Coulomb-fitting basis sets for H to Rn,” *Physical Chemistry Chemical Physics* 8 (2006): 1057–1065.

79. S. Hirata and M. Head-Gordon, “Time-Dependent Density Functional Theory within the Tamm-Dancoff Approximation,” *Chemical Physics Letters* 314 (1999): 291–299.

80. A. Hellweg, C. Hättig, S. Höfener, and W. Klopper, “Optimized Accurate Auxiliary Basis Sets for RI-MP2 and RI-CC2 Calculations for the Atoms Rb to Rn,” *Theoretical Chemistry Accounts* 117 (2007): 587–597.

81. M. Casanova-Páez and L. Goerigk, “Time-Dependent Long-Range-Corrected Double-Hybrid Density Functionals with Spin-Component and Spin-Opposite Scaling: A Comprehensive Analysis of Singlet-Singlet and Singlet-Triplet Excitation Energies,” *Journal of Chemical Theory and Computation* 17 (2021): 5165–5186.

82. C. Angeli, R. Cimiraglia, and J.-P. Malrieu, “N-Electron Valence State Perturbation Theory: A Spinless Formulation and an Efficient Implementation of the Strongly Contracted and of the Partially Contracted Variants,” *The Journal of Chemical Physics* 117 (2002): 9138–9153.

83. G. Henkelman and H. Jónsson, “Improved Tangent Estimate in the Nudged Elastic Band Method for Finding Minimum Energy Paths and Saddle Points,” *The Journal of Chemical Physics* 113 (2000): 9978–9985.

84. V. Á. Sgeirsson, B. O. Birgisson, R. Bjornsson, et al., “Nudged Elastic Band Method for Molecular Reactions Using Energy-Weighted Springs Combined with Eigenvector Following,” *Journal of Chemical Theory and Computation* 17 (2021): 4929–4945.

85. K. Ishida, K. Morokuma, and A. Komornicki, “The Intrinsic Reaction Coordinate. An Ab Initio Calculation for HNC->HCN and $H+CH_4$->CH_4+H-,” *The Journal of Chemical Physics* 66 (1977): 2153–2156.

86. V. Barone and M. Cossi, “Quantum Calculation of Molecular Energies and Energy Gradients in Solution by a Conductor Solvent Model,” *The Journal of Physical Chemistry. A* 102 (1998): 1995–2001.

87. M. Garcia-Rates and F. Neese, “Effect of the Solute Cavity on the Solvation Energy and its Derivatives within the Framework of the Gaussian Charge Scheme,” *Journal of Computational Chemistry* 41 (2020): 922–939.

88. B. de Souza, F. Neese, and R. Izsák, “On the Theoretical Prediction of Fluorescence Rates from First Principles using the Path Integral Approach,” *The Journal of Chemical Physics* 148 (2018): 034104.

89. Q. Peng, Y. Yi, Z. Shuai, and J. Shao, “Excited State Radiationless Decay Process with Duschinsky Rotation Effect: Formalism and Implementation,” *The Journal of Chemical Physics* 126 (2007): 114302.

90. R. R. Valiev, V. Cherepanov, R. Nasibullin, D. Sundholm, and T. Kurtén, “Calculating Rate Constants for Intersystem Crossing and

Internal Conversion in the Franck-Condon and Herzberg-Teller Approximations," *Physical Chemistry Chemical Physics* 21 (2019): 18495–18500.

91. A.-R. Allouche, "Gabedit — A Graphical User Interface for Computational Chemistry Softwares," *Journal of Computational Chemistry* 32 (2011): 174–182.

92. M. D. Hanwell, D. E. Curtis, D. C. Lonie, T. Vandermeersch, E. Zurek, and G. R. Hutchison, "Avogadro: An Advanced Semantic Chemical Editor, Visualization, and Analysis Platform," *Journal of Cheminformatics* 4 (2012): 17.

93. R. Dennington, T. Keith, and J. Millam, Gaussview 6.1.1. (semichem Inc, 2009).

Supporting Information

Additional supporting information can be found online in the Supporting Information section. **Supporting Fig. S1:** The $R_e(S_0)^{SP}$ equilibrium geometry computed at DFT/ωB97X-D3BJ/def2-TZVPP level of theory. **Supporting Fig. S2:** The $R_e(S_1)^a$ equilibrium geometry computed at TDDFT/ωB97X-D3BJ/def2-TZVPP level of theory. **Supporting Fig. S3:** The $ci(S_3 \times S_2)$ conical intersection geometry computed at TDDFT/ωB97X-D3BJ/def2-TZVPP level of theory. **Supporting Fig. S4:** The $ci(S_2 \times S_1)$ conical intersection geometry computed at TDDFT/ωB97X-D3BJ/def2-TZVPP level of theory. **Supporting Fig. S5:** The $R_e(S_1)^b$ equilibrium geometry computed at TDDFT/ωB97X-D3BJ/def2-TZVPP level of theory. **Supporting Fig. S6:** The $R_e(S_1)^c$ equilibrium geometry computed at TDDFT/ωB97X-D3BJ/def2-TZVPP level of theory. **Supporting Fig. S7:** The TS^1 transition state geometry between the $R_e(S_1)^b$ and $R_e(S_1)^c$ equilibrium geometries computed at NEB/TDDFT/ωB97X-D3BJ/def2-TZVPP level of theory. **Supporting Fig. S8:** The $ci(S_0 \times S_1)^a$ conical intersection geometry computed at SF-TDDFT/ωB97X-D3BJ/def2-TZVPP level of theory. **Supporting Fig. S9:** The $ci(S_0 \times S_1)^i$ conical intersection geometry of benzopyran computed at SF-TDDFT/ωB97X-D3BJ/def2-TZVPP level of theory. **Supporting Fig. S10:** The $ci(S_0 \times S_1)^i$ conical intersection geometry of 6-nitro benzopyran computed at SF-TDDFT/ωB97X-D3BJ/def2-TZVPP level of theory. **Supporting Fig. S11:** The $ci(S_0 \times S_1)^b$ conical intersection geometry computed at SF-TDDFT/ωB97X-D3BJ/def2-TZVPP level of theory. **Supporting Fig. S12:** The $ci(S_0 \times S_1)^{ii}$ conical intersection geometry of benzopyran computed at SF-TDDFT/ωB97X-D3BJ/def2-TZVPP level of theory. **Supporting Fig. S13:** The $ci(S_0 \times S_1)^{ii}$ conical intersection geometry of 6-nitro benzopyran computed at SF-TDDFT/ωB97X-D3BJ/def2-TZVPP level of theory. **Supporting Fig. S14:** The $R_e(S_0)^{MC}$ equilibrium geometry computed at DFT/ωB97X-D3BJ/def2-TZVPP level of theory. **Supporting Fig. S15:** The $R_e(S_0)^{SP}$ equilibrium geometry computed at DFT/ωB97X-D3BJ/def2-TZVPP/CPCM(water) level of theory. **Supporting Fig. S16:** The $R_e(S_1)^a$ equilibrium geometry computed at TDDFT/ωB97X-D3BJ/def2-TZVPP/CPCM(water) level of theory. **Supporting Fig. S17:** The $ci(S_1 \times S_2)$ conical intersection geometry computed at TDDFT/ωB97X-D3BJ/def2-TZVPP/CPCM(water) level of theory. **Supporting Fig. S18:** The $R_e(S_1)^b$ equilibrium geometry computed at TDDFT/ωB97X-D3BJ/def2-TZVPP/CPCM(water) level of theory. **Supporting Fig. S19:** The TS^1 transition state geometry between the $R_e(S_1)^b$ and $R_e(S_1)^c$ equilibrium geometries computed at NEB/TDDFT/ωB97X-D3BJ/def2-TZVPP/CPCM(water) level of theory. **Supporting Fig. S20:** The $R_e(S_1)^c$ equilibrium geometry computed at TDDFT/ωB97X-D3BJ/def2-TZVPP/CPCM(water) level of theory. **Supporting Fig. S21:** The TS^2 transition state geometry between the $R_e(S_1)^c$ and $R_e(S_1)^d$ equilibrium geometries computed at NEB/TDDFT/ωB97X-D3BJ/def2-TZVPP/CPCM(water) level of theory. **Supporting Fig. S22:** The $R_e(S_1)^d$ equilibrium geometry computed at TDDFT/ωB97X-D3BJ/def2-TZVPP/CPCM(water) level of theory. **Supporting Fig. S23:** The $R_e(S_0)^{MC}$ equilibrium geometry computed at DFT/ωB97X-D3BJ/def2-TZVPP/CPCM(water) level of theory. **Supporting Fig. S24:** The $ci(S_1 \times S_0)^a$ conical intersection geometry computed at SF-TDDFT/ωB97X-D3BJ/def2-TZVPP/CPCM(water) level of theory. **Supporting Fig. S25:** The $ci(S_1 \times S_0)^b$ conical intersection geometry computed at SF-TDDFT/ωB97X-D3BJ/def2-TZVPP/CPCM(water) level of theory. **Supporting Fig. S26:** The $ci(S_0 \times S_1)^c$ conical intersection geometry computed at SF-TDDFT/ωB97X-D3BJ/def2-TZVPP level of theory. **Supporting Fig. S27:** The TS^3 transition state geometry between the $R_e(S_0)^{SP}$ and $R_e(S_0)^{MC}$ equilibrium geometries computed at NEB/TDDFT/ωB97X-D3BJ/def2-TZVPP level of theory. **Supporting Fig. S28:** The TS^3 transition state geometry between the $R_e(S_0)^{SP}$ and $R_e(S_0)^{MC}$ equilibrium geometries computed at NEB/TDDFT/ωB97X-D3BJ/def2-TZVPP/CPCM(water) level of theory. **Supporting Fig. S29:** The $R_e(S_1)^d$ equilibrium geometry computed at TDDFT/ωB97X-D3BJ/def2-TZVPP level of theory. **Supporting Fig. S30:** The TS^2 transition state geometry between the $R_e(S_1)^c$ and $R_e(S_1)^d$ equilibrium geometries computed at NEB/TDDFT/ωB97X-D3BJ/def2-TZVPP level of theory. **Supporting Fig. S31:** The C_1–C_2, C_2–C_3 and C_3–C_4 bond lengths during the IRC calculation and geometry optimization in vacuum (ωB97X-D3BJ/def2-TZVPP). **Supporting Fig. S32:** The C_1–C_2, C_2–C_3 and C_3–C_4 bond lengths during the IRC calculation and geometry optimization in polar environment (ωB97X-D3BJ/def2-TZVPP/CPCM(water)). **Supporting Fig. S33:** The $R_e(T_1)^a$ equilibrium geometry computed at TDDFT/ωB97X-D3BJ/def2-TZVPP level of theory. **Supporting Fig. S34:** The $R_e(T_1)^a$ equilibrium geometry computed at TDDFT/ωB97X-D3BJ/def2-TZVPP/CPCM(water) level of theory. **Supporting Fig. S35:** The $R_e(T_1)^c$ equilibrium geometry computed at TDDFT/ωB97X-D3BJ/def2-TZVPP level of theory. **Supporting Fig. S36:** The $R_e(T_1)_c$ equilibrium geometry computed at TDDFT/ωB97X-D3BJ/def2-TZVPP/CPCM(water) level of theory. **Supporting Fig. S37:** The $R_e(T_1)^d$ equilibrium geometry computed at TDDFT/ωB97X-D3BJ/def2-TZVPP level of theory. **Supporting Fig. S38:** The $R_e(T_1)^d$ equilibrium geometry computed at TDDFT/ωB97X-D3BJ/def2-TZVPP/CPCM(water) level of theory. **Supporting Fig. S39:** The $R_e(T_2)^c$ equilibrium geometry computed at TDDFT/ωB97X-D3BJ/def2-TZVPP level of theory. **Supporting Fig. S40:** The $R_e(T_2)^c$ equilibrium geometry computed at TDDFT/ωB97X-D3BJ/def2-TZVPP/CPCM(water) level of theory. **Supporting Fig. S41:** The $R_e(T_2)^d$ equilibrium geometry computed at TDDFT/ωB97X-D3BJ/def2-TZVPP level of theory. **Supporting Fig. S42:** The $R_e(T_2)^d$ equilibrium geometry computed at TDDFT/ωB97X-D3BJ/def2-TZVPP/CPCM(water) level of theory. **Supporting Table S1:** The natural difference orbitals (NDOs) between the ground and the given electronic excited state computed for the Spiropyran at **M1**: TDDFT/ωB97X-D3BJ/def2-TZVPP/(vacuum) level of theory (red = hole, cyan = electron density). **Supporting Table S2:** The natural difference orbitals (NDOs) between the ground and the given electronic excited state computed for the Spiropyran at **M2**: TDDFT/ωB97X-D3BJ/def2-TZVPP/CPCM(water) level of theory (red = hole, cyan = electron density). **Supporting Table S3:** The natural difference orbitals (NDOs) between the ground and the given electronic excited state computed for the Spiropyran at **M3**: TDDFT/SOS-PBE-QIDH/def2-TZVPP/(vacuum) level of theory (red = hole, cyan = electron density). **Supporting Table S4:** The natural difference orbitals (NDOs) between the ground and the given electronic excited state computed for the Spiropyran at **M4**: TDDFT/SOS-PBE-QIDH/def2-TZVPP/CPCM(water) level of theory (red = hole, cyan = electron density). **Supporting Table S5:** The first five electronic excited state wavelengths (in nm) of MC, their oscillator strengths (in parenthesis) and their fragment localization computed at four level of theories: **M1** - ωB97X-D3BJ/def2-TZVPP/(vacuum), **M2** - ωB97X-D3BJ/def2-TZVPP/CPCM(water), **M3** - SOS-PBE-QIDH/def2-TZVPP/(vacuum) and **M4** - SOS-PBE-QIDH/def2-TZVPP/CPCM(water). **Supporting Table S6:** The natural difference orbitals (NDOs) between the ground and the given electronic excited state computed for the Merocyanine at **M1**: TDDFT/ωB97X-D3BJ/def2-TZVPP/(vacuum) level of theory (red = hole, cyan = electron density). **Supporting Table S7:** The natural difference orbitals (NDOs) between the ground and the given electronic excited state computed for the Merocyanine at **M2**: TDDFT/ωB97X-D3BJ/def2-TZVPP/(water) level of theory (red = hole, cyan = electron density). **Supporting Table S8:** The natural difference orbitals (NDOs) between the ground and the given electronic excited state computed for the Merocyanine at **M3**: TDDFT/SOS-PBE-QIDH/def2-TZVPP/(vacuum) level of theory (red = hole, cyan = electron density). **Supporting Table S9:** The natural difference orbitals (NDOs) between the ground and the given electronic excited state computed for the Merocyanine at **M4**: TDDFT/SOS-PBE-QIDH/def2-TZVPP/(water) level of theory (red = hole, cyan = electron density).